Modeling the Oxygen Reduction Reaction on Nitrogen-Doped Graphene

Robert Warburton
The Ohio State University

Presented in partial fulfillments for Graduation with Honors Research Distinction in Chemical & Biomolecular Engineering

Honors Thesis Committee:

Dr. Aravind Asthagiri
Dr. Umit Ozkan

Abstract

Atmospheric carbon dioxide levels are higher than they have been in the last million years. The environmental concerns associated with anthropogenic carbon pollution have motivated investment in alternative energy sources. Polymer electrolyte membrane fuel cells (PEMFCs) are one such candidate, utilizing hydrogen as the energy carrier. However, the sluggish kinetics of the oxygen reduction reaction (ORR) at the cell cathode and the high cost of the platinum catalyst are the main barriers to commercialization. As a result, much effort has gone into investigating non-precious metal catalytic materials to reduce platinum loading. Experimentally, nitrogen-doped graphene materials (CN_x) have shown promise for their ORR activity. However, the chemical nature of the active site is subject to much debate. This study utilizes density functional theory (DFT) to model the elementary steps of the ORR on CN_x. The free energies of each reaction intermediate are used to derive the onset potential, where current is experimentally observable. Water molecules are explicitly included in the model to simulate solvation at the cathode. These results are used to evaluate the application of solvation corrections developed for Pt(111). Following the introduction of a water bilayer into the system, the results exhibit relative agreement to the proposed constant solvation corrections, but are quantitatively variant. These findings suggest that the Pt(111) solvent corrections do not entirely translate to these materials, and the explicit inclusion of water may be necessary to properly evaluate solvent effects on the ORR activity of CNx. The extension of these methods to modeling on nitrogen defects on graphene edge sites and TM-CN_x surfaces is discussed.

Acknowledgements

I would like to thank Dr. Aravind Asthagiri for giving me the opportunity to conduct research in his group. I have learned how to think critically through my time in the group, while given the opportunity to work independently on a project of great interest to me. The guidance I have received along will be invaluable for my future endeavors. I would also like to thank Mehak Chawla and Wenjia Luo for helping to teach me the computational methods necessary to perform the experiments for my research.

I would also like to thank my family and friends for their unwavering love and support. The encouragement I have received from those closest to me has been my greatest motivator.

Table of Contents

List of Figures

List of Tables

1. Introduction

1.1 – Alternative Energy

All human activity is dependent on energy. As population increases, worldwide energy demand continues to amplify. With a significant majority of human energy needs being satisfied by fossil resources, such as petroleum and coal, the increasing energy demand is cause for concern with respect to depletion and environmental impacts.

Through observation of the peak production capacity of a single oil well, M. King Hubbert proposed the concept of "peak oil" in the 1950's. Hubbert scaled his observation up to the level of oil production capacity of the entire United States, hypothesizing a peak in oil production around 1970. Beyond this peak, production capacity will not be able to keep up with demand [1]. This concept is illustrated in Figure 1. In fact, Hubbert correctly predicted this peak in production, which occurred around 1970. United States field production of oil has been increasing recently due to increases in shale gas production. However, this only succeeds in suspending this peak, which exist for any resource that is not replenished at a rate greater than or equal to its rate of consumption.

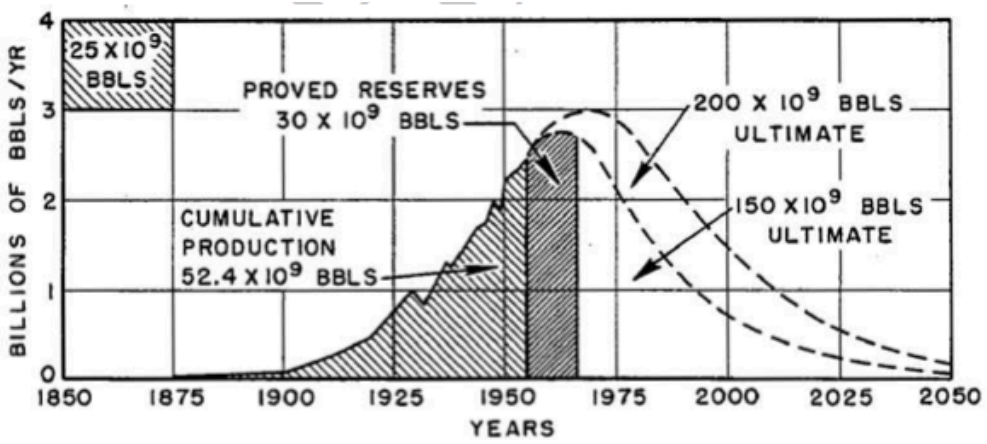

Figure 1. Hubbert's prediction about United States oil production peak [1].

In addition to concerns with depletion, there exist many environmental concerns with fossil fuel consumption. The current state of the carbon cycle is depicted in Figure 2, where carbon sources are utilized by humans, resulting in emissions of carbon dioxide into the atmosphere. The amount of CO_2 emitted into the atmosphere far exceeds sequestration capacity of plants, disrupting the composition of the atmosphere.

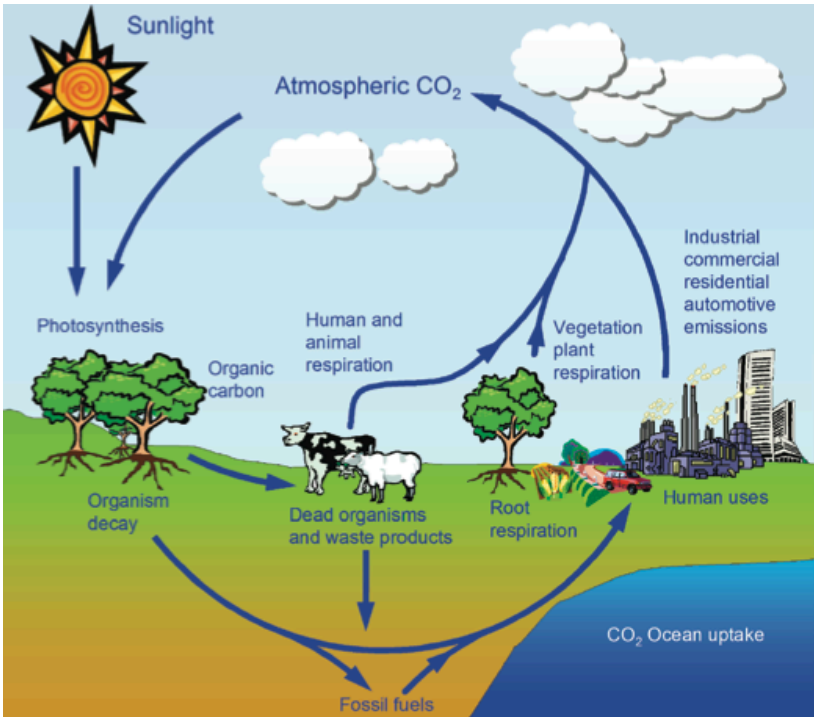

Figure 2. Unsustainable carbon cycle [2]

Figure 3 described the dynamics of atmospheric CO_2 concentrations over the last 800,000 years. Although the CO_2 concentration has typically cycled between 200 and 300 ppm, current measurements indicate atmospheric levels exceeding 400 ppm, providing strong evidence for the impact of anthropogenic industrialization on atmospheric concentrations. CO_2 is the primary greenhouse gas in the atmosphere, disrupting the energy balance of the Earth, and contributing to global climate change [3].

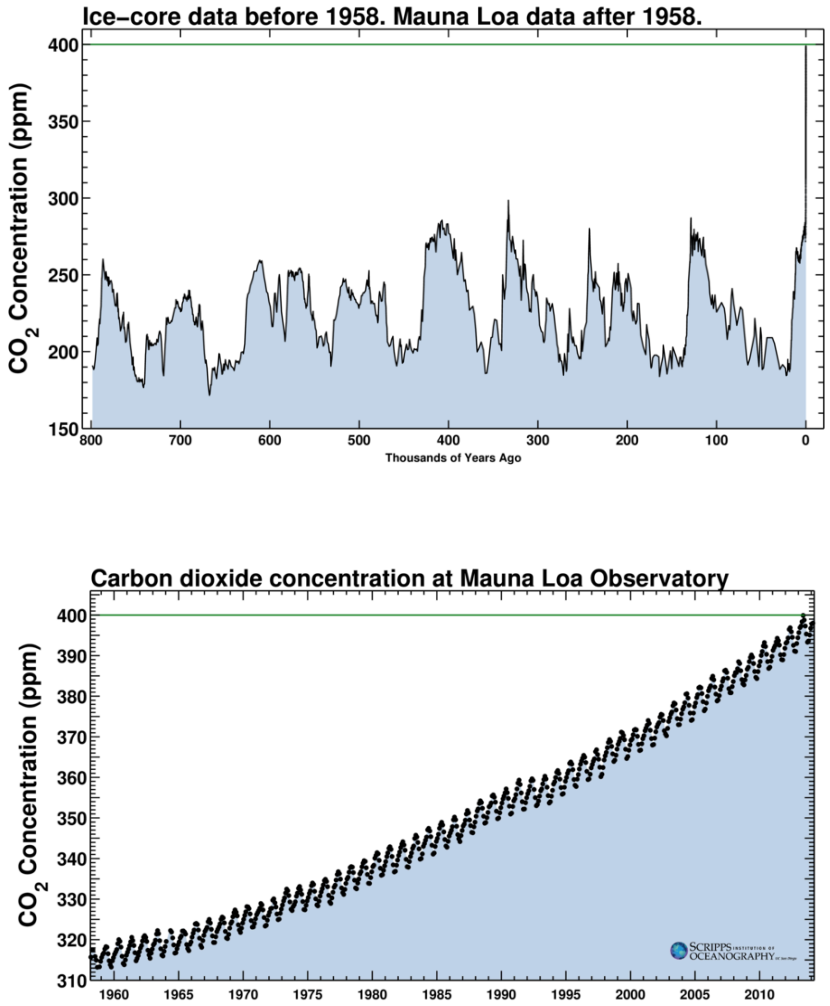

Figure 3. Atmospheric CO_2 concentrations over the last **(top)** 800,000 years, and **(bottom)** 60 years [4]

Increased public awareness regarding the negative implications of climate change has motivated the search for means of reducing the impact of humans on atmospheric conditions. Such efforts may involve the capture of CO2 and converting it into methane or liquid fuels[5]. Methods of energy production that present reduced, or even zero, direct CO_2 emissions are also becoming increasingly attractive [6]. These approaches may contribute to a more sustainable

global carbon cycle, similar to the flow diagram in Figure 4. Fuel cell technology is a promising direction for sustainable energy production, providing the opportunity to generate electricity with a reduced carbon footprint.

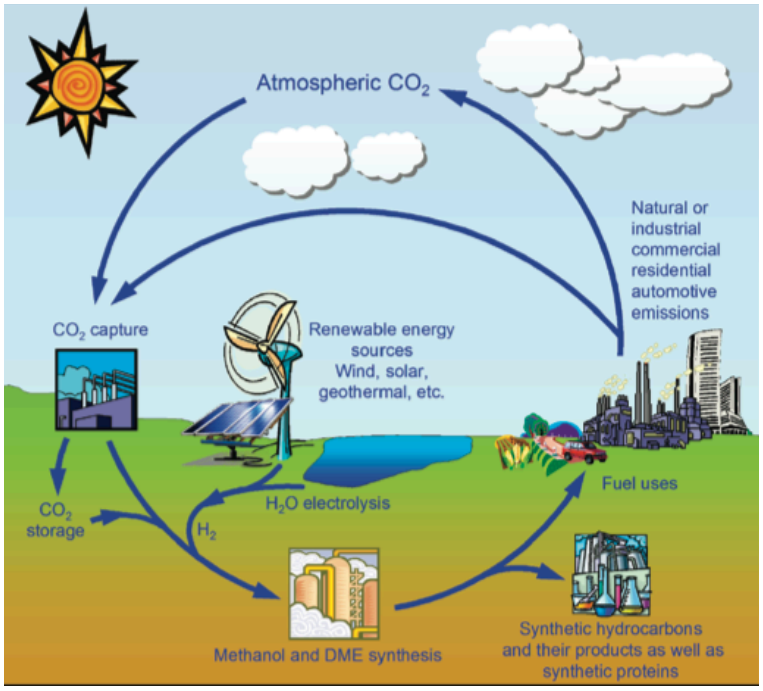

Figure 4. Sustainable carbon cycle [2]

1.2 – PEMFC Overview

Polymer electrolyte membrane fuel cells (PEMFCs) utilize hydrogen as an energy carrier and directly convert chemical energy to electricity. They are capable of operating at high efficiencies compared to the conventional combustion engine, since they are not limited by the Carnot cycle efficiency [7]. These systems have potential to be utilized in both mobile and stationary energy production applications. A process flow diagram for typical fuel cell stack operation is included in Figure 5.

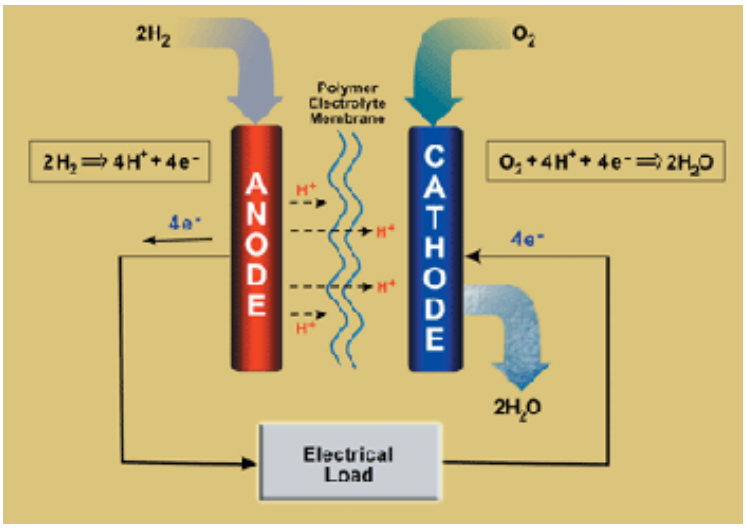

Figure 5. Process flow diagram for a hydrogen fuel cell [8]

The fuel cell has an anode and cathode, which are separated by a polymer membrane. Hydrogen gas is fed into the system at the anode, where it is broken down into protons and electrons. The protons are selectively transported across the membrane, whereas the electrons are diverted through a circuit in order to generate current for the cell. The cathodic oxygen reduction reaction (ORR) involves the reaction of protons and electrons with oxygen to generate water, releasing energy. The overall reaction in the fuel cell, with a ΔG_{rxn} = -2.46 eV/molecule H_2, is represented by the following:

$$H_2 + ½\ O_2 \rightarrow 2\ H_2O \qquad (1)$$

The majority of hydrogen production occurs through steam reforming of hydrocarbons. However, water electrolysis is an opportunity to generate hydrogen independent of fossil resources [9]. As depicted in the sustainable carbon cycle in Figure 4, utilizing renewable sources of energy, such as solar or wind energy for hydrogen production through hydrolysis, would contribute to a lesser carbon footprint for the life cycle of a fuel cell.

1.3 – Challenges

Although fuel cell technology is attractive for its potential benefits to global energy infrastructure, there exist barriers to large-scale commercialization. The main technological barrier involves the sluggish kinetics of the ORR at the cathode. The ORR contributes to significant decreases in fuel cell efficiency [10].

The best cathode catalysts also involve significant integration of platinum, which is scarce and expensive. Figure 6 demonstrates the dominance of anthropogenic mobilization of platinum, along with other precious and rare earth metals, utilized in catalysis [11]. Though these elements have superior catalytic capabilities, the consumption rate is high. This presents potential depletion issues, which are likely to increase their costliness.

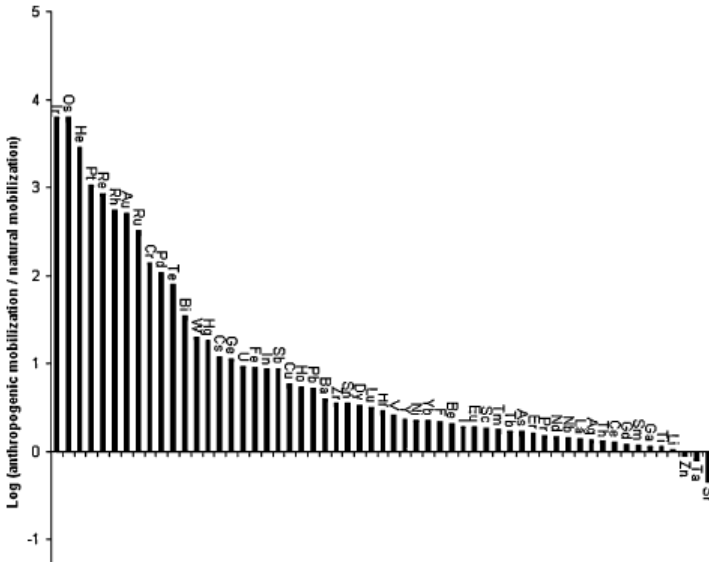

Figure 6. Ratio of anthropogenic and natural mobilization flows of several elements [11]

Analysis has shown that the platinum in fuel cells may account for as much as half the cost of a fuel cell stack [12]. This has motivated researchers to investigate candidate catalytic materials for the ORR that may reduce the required platinum loading in fuel cells. As shown in Figure 7, recent research has identified platinum alloys that exhibit high activity for the ORR. However, it is unlikely that these alloys will exhibit the stability to operate long-term in the corrosive environment of a fuel cell [13].

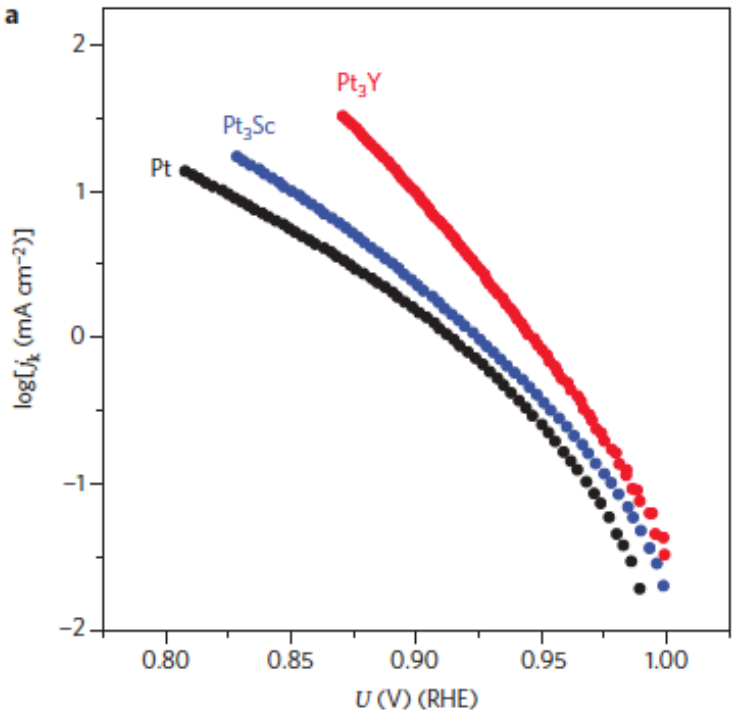

Figure 7. Specific activity of Pt, Pt_3Sc, Pt_3Y towards the ORR [13].

1.4 – CN_x Materials

Nitrogen-doped graphene (CN_x) materials have been identified through experiment to be stable, active ORR catalysts [14-16]. Figure 8 demonstrates these properties. Figure 8a compares the ORR activity of CN_x with a commercial Pt/C catalyst. The polarization curve indicates that the CN_x onset potential is competitive with the Pt/C catalyst, which is representative of the

catalytic activity of the materials. Figure 8b demonstrates the stability of the CN_x current density after numerous cycles, and the insert of 8b shows the consistency of the cathodic oxygen reduction peaks over 500 potential sweep cycles. Each of these figures demonstrates the superior stability in the CN_x materials, compared to the commercial Pt/C catalyst [15].

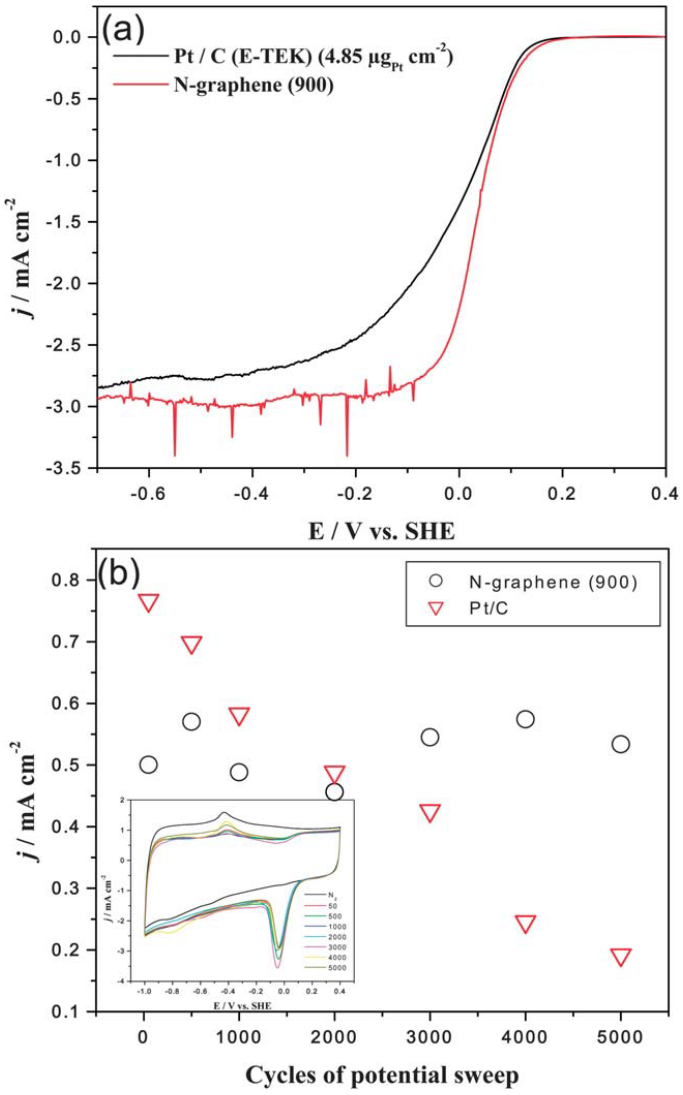

Figure 8. (a) Polarization curves, **(b)** durability tests **(insert)** cyclic voltammograms after various potential sweep cycles for CN_x and Pt/C [15].

Since these materials demonstrate the ability to be competitive with the activity of platinum-based ORR catalysts, their potential integration into fuel cells is promising. CN_x

presents a much more economical alternative to the costly precious-metal materials that are currently utilized in commercial fuel cell stacks. However, there is still much to be understood regarding the source of activity in these materials. The role of nitrogen towards the catalytic activity is subject to much debate, due to the various potential nitrogen defect patterns [17] and the transition metal precursors involved in synthesis [16,18-25].

It is understood that the more electronegative nitrogen defect draws electron density away from adjacent carbon atoms, lowering O_2 adsorption barriers and increasing adsorption energies of the ORR reaction intermediates [26]. Further atomistic modeling of the ORR on these materials may elucidate the chemical nature of the active site.

1.5 – Solvent Effects in Theoretical Models

Although there have been several modeling studies of the ORR on CN_x [17,27,28], previous work has neglected to explicitly model the role of the solvent towards the predicted catalytic activity. Implicit solvent corrections have been developed previously for the ORR [29-31]. However, these corrections have been established for Pt(111) and other precious metals, and may not directly translate to CN_x materials. The electronic structure of graphene-based materials is much different than that of metals, so the degree of error in applying these implicit corrections to the CN_x system may be quite significant.

This study is conducted in order to understand the role of the solvent in the ORR mechanism in these materials. Using first-principles calculations, based on quantum mechanics, the elementary steps of the ORR are modeled on a CN_x surface with the explicit inclusion of water molecules. This is carried out in order to provide an understanding of the reaction scheme

at the atomic level, which can be used to further motivate the design of robust materials for catalyzing oxygen reduction.

2. Experimental Methods

2.1 – Electronic Structure Calculations

The Vienna *ab initio* simulation package (VASP) is utilized to perform the Density Functional Theory (DFT) calculations in this work [32-35]. The electronic structure calculations use projector augmented wave (PAW) psuedopotentials [36,37], and the Perdew-Burke-Ernzerhof (PBE) exchange-correlation functional [38] with a plane-wave cutoff of 400 eV. The residual minimization method from direct inversion in the iterative subspace (RMM-DIIS) relaxation is used, with a preconditioned residuum minimization subswitch. Simulations utilize Fermi smearing with a Gaussian width of 0.1 eV. The force constraint between all atoms is 0.03 eV/Å.

Due to the inclusion of water molecules in the model, it is essential to include dispersion corrections in order to accurately describe H_2O-graphene adsorption energies and equilibrium distances [39,40]. Traditional DFT has difficulty describing these properties, but the inclusion of dispersion corrections more accurately reflects results calculated by higher order calculations [41]. Therefore, the DFT-D3 correction developed by Grimme and co-workers is incorporated to describe the van der Waals interactions in the model [42].

2.2 - Modeling the CN_x surface

The surface is modeled as a two-dimensional periodic slab defined by 18 atoms (17 carbon, 1 nitrogen defect). The unit cell is included in Figure 9. Adsorbate interactions occur

when modeling the ORR on the 3 x 3 unit cells, impacting the predicted adsorption energies. The adsorption energies converge when the cell size is doubled in each direction, to a 6 x 6 supercell. The Brillouin zone is sampled with a 4 x 4 x 1 and 2 x 2 x 1 k-point Monkhorst-Pack k-point mesh for the 3 x 3 and 6 x 6 cells, respectively.

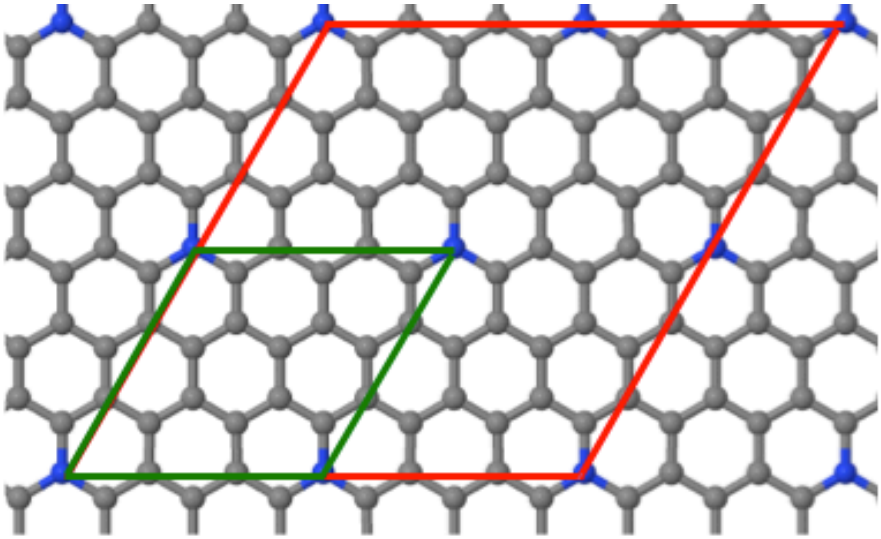

Figure 9. Structures of 3x3 and 6x6 CN_x supercells

2.3 – Potential-Dependent Free Energies

The ground state energy is calculated from the output of the converged DFT calculations. However, the free energy is necessary to understand the thermodynamics of the reaction scheme. The vibrational modes are determined through DFT, and statistical mechanics uses the vibrational modes to calculate entropic contributions to the free energy of the system. Each of the vibrational modes is positive to ensure that the system is at a minimum energy state, rather than a saddle on the potential energy surface. The energy of O_2 is not described accurately. Therefore, the free energy used for this molecule is corrected according to the overall water-splitting reaction thermodynamics as is done elsewhere [9,28].

In order to derive the predicted onset potential for the fuel cell system, it is necessary to determine the potential dependence of the free energy of each state in the reaction scheme. In order to account for the effect of the cell potential, the linear free energy method is utilized [29]. Through this assumption, the free energy of a proton-electron pair is equal to half the free energy of an H_2 molecule at 0 V-RHE. All proton-electron transfer steps account for potential dependence by shifting the free energy by $-eU$, where e is the electronic charge of an electron and U is the applied potential, in V-RHE. The free energy of reaction (ΔG_{rxn}) for each reduction step in the reaction scheme is then calculated by the following:

$$\Delta G_{rxn}(U) = \Delta G_{rxn}(0 \text{ V-RHE}) - eU \quad (2)$$

The linear free energy method defines the onset potential to be the maximum potential where each step in the reaction scheme is downhill ($\Delta G_{rxn} < 0$). The overpotential is defined as the difference between the onset potential and the equilibrium potential (U_0 = 1.23 V, as determined by the thermodynamics of the overall reaction):

$$\eta = U_0 - U \quad (3)$$

The optimal catalyst will operate the equilibrium potential of 1.23 V (zero overpotential). This only occurs if the ΔG_{rxn} between each step in the reaction scheme is 1.23 eV at 0 V – RHE, and the $\Delta G_{rxn} = 0$ at an applied potential of 1.23 V.

3. Results and Discussion

3.1 – Modeling the ORR Without Solvent Effects

The most favorable adsorption site (greatest adsorption energy) for each of the intermediates in the reaction scheme is determined to be the carbon atom adjacent to the nitrogen defect. The geometries of the adsorbed species are indicated in Figure 10. These calculations are

converged with the 6 x 6 unit cell, due to adsorbate interactions over the periodic boundary in smaller cell sizes.

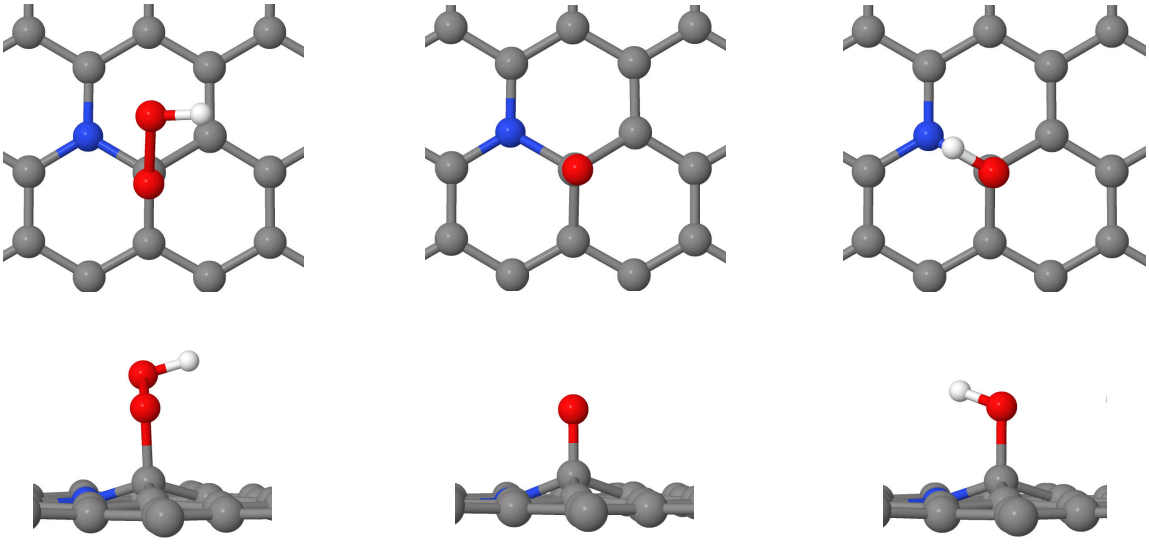

Figure 10. Reaction intermediates: (left to right) OOH*, O*, and OH*

The free energies of each step in the reaction sequence are calculated at 0 V-RHE, and subsequently corrected according to the applied potential by the methods described previously. These calculations are used to generate the free energy diagram in Figure 11 by taking all calculated free energies relative to the free energy of the overall reaction product (2 molecules H_2O).

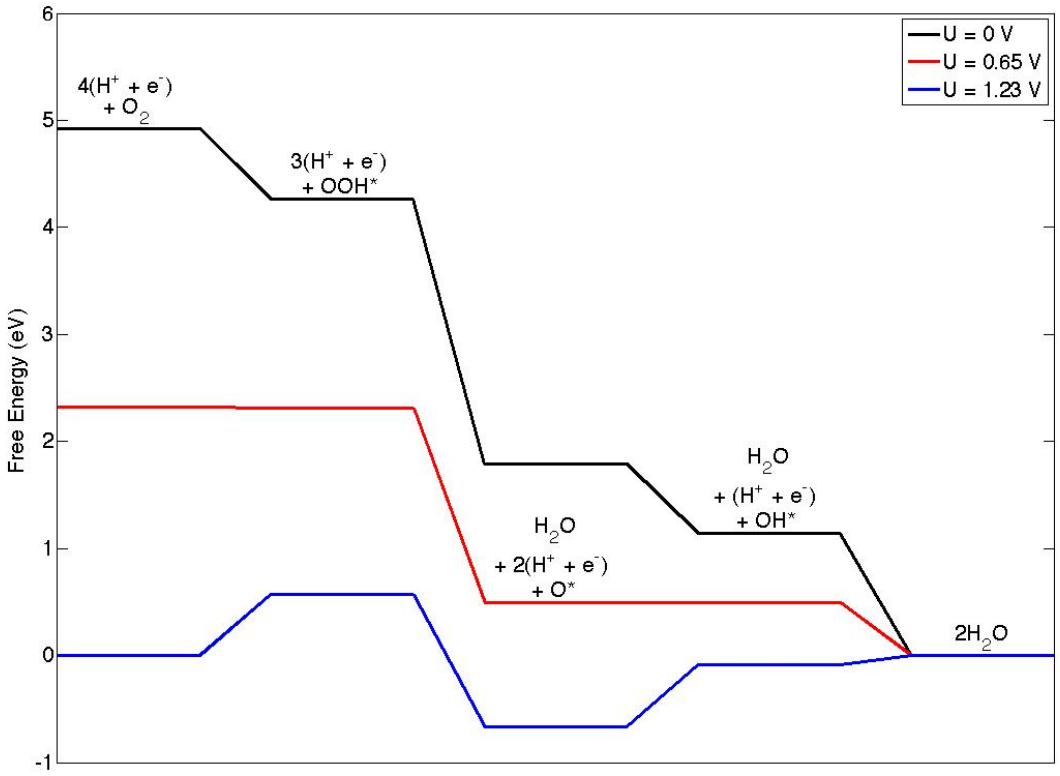

Figure 11. Free energy diagram omitting solvent interactions

Each step in the reaction scheme is downhill at 0 V – RHE, indicating thermodynamic favorability between each of the steps in the sequence from reactants to overall products. The OOH* intermediate is downhill by 0.66 eV relative to the reactant. Reduction of the OOH* to O*, releasing a water molecule in the process is downhill by 2.46 eV. The following proton-electtron transfer, resulting in an adsorbed OH* intermediate is lowered in energy by 0.66 eV. The final reduction of this adsorbed specie to water results in a free energy change of 1.14 eV.

Applying potential to the system allows for derivation of the onset potential. At the equilibrium potential of 1.23 V, it is determined that the OOH* intermediate is underbound with respect to the optimal ORR catalyst, where as the O* and OH* species are overbound. This results in several uphill steps at this potential, which predicts incomplete reduction. The onset

potential is determined to be at 0.65 V. This is the greatest potential at which all reaction steps are downhill, limited by the reduction of O* to OH* where the $\Delta G_{rxn} = 0$. This prediction differs from a similar study. However, differences in predicted overpotential and rate-determining step can likely be attributed to different funcitonals utilized between the studies [28]. The calculations therefore predict this reduction step to be the rate-limiting step in the reaction sequence. The assumption of the linear free energy method is that given these conditions, barriers between steps can easily be overcome at room temperature.

3.2 – Implicit Solvent Corrections

Applying solvent corrections to the calculated free energies of each reaction intermediate will likely provide further stabilization (greater adsorption energies) to the OOH* and OH* intermediates. The corrections developed for Pt(111) indicate that these stabilization effects should be approximately 0.25 eV and 0.50 eV for OOH* and OH*, respectively [29-31]. These implicit corrections are factored into the calculations represented in Figure 11 to determine the impact of their inclusion on the predicted catalyst activity. The adjustments to these calculations are used to generate the energy diagram included in Figure 12.

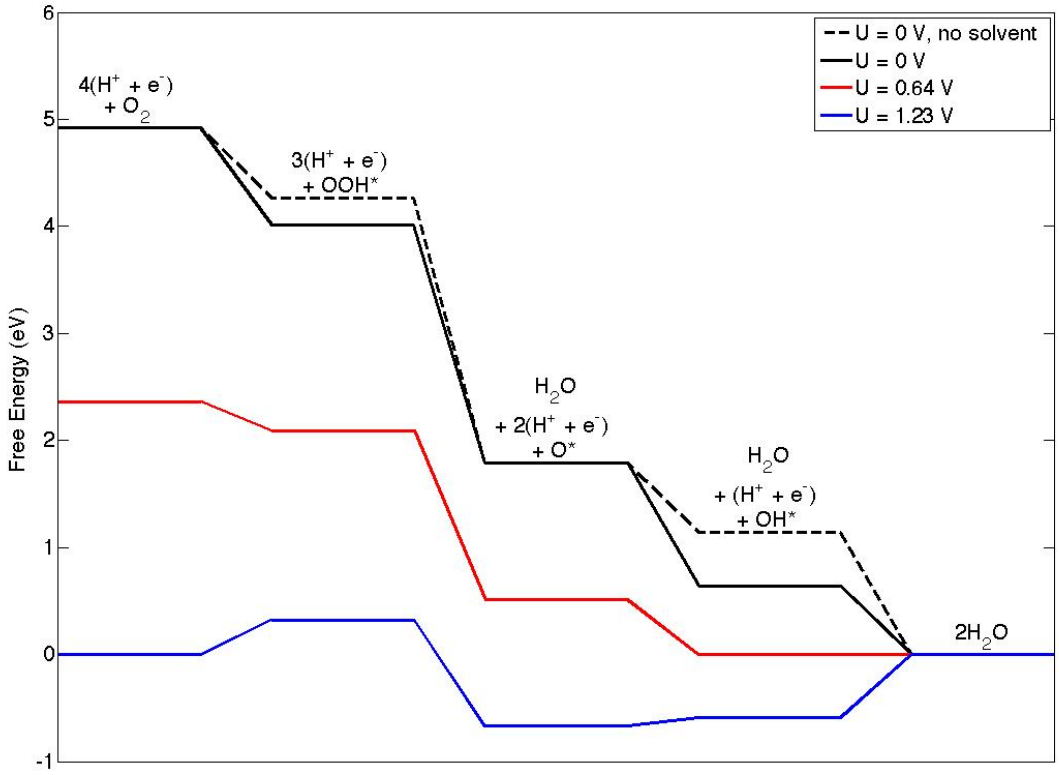

Figure 12. Free energy diagram including constant solvent corrections

The stabilization correction of 0.25 eV on the OOH* intermediate is favorable with respect to the optimal ORR catalyst since the intermediate was determined to be underbound without any correction for solvent interactions. However, the OH* intermediate was predicted to be overbound without solvent corrections. The stabilization of 0.50 eV as predicted by the implicit corrections is an unfavorable adjustment to the intermediate free energy. In fact, at 0.64 V the final reduction has a $\Delta G_{rxn} = 0$, suggesting that this is the rate-limiting step.

Because of the impact of the solvent correction on the overbound OH* specie, there is an insignificant change in the predicted overpotential with the inclusion of solvent corrections. However, CN_x materials have a much different electronic structure than Pt(111), the surface for which these corrections have been established. Thus, it is important to investigate the role of

explicit solvent inclusion in these theoretical models to better understand these fundamental properties of the system. The implementation of explicit solvent corrections will be discussed further in the subsequent sections.

3.3 – Water Structure on CN_x

Previous theoretical [31,43] and experimental [44] surface science studies of water on graphene indicate energetic favorability with water exhibiting acceptor characteristics. However, additional work suggests that stabilization effects by the surface are much less than those provided by hydrogen bonding interactions between multiple water molecules [32]. This demonstrates the magnitude of the surface hydrophobicity. With the introduction of the nitrogen defect, the electronic structure of the surface is modified. Thus, it is important to evaluate these previous findings to determine if the structural characteristics of the solvent will be similar with the inclusion of the nitrogen defect.

The solvent layer is modeled as a hexagonal ice bilayer on the surface of CN_x. Two general configurations of the bilayer are considered: one in which a hydrogen atom points away from the surface (H-up), and one in which a hydrogen atom is coordinated directly towards the surface (H-down). These configurations are illustrated in Figure 13.

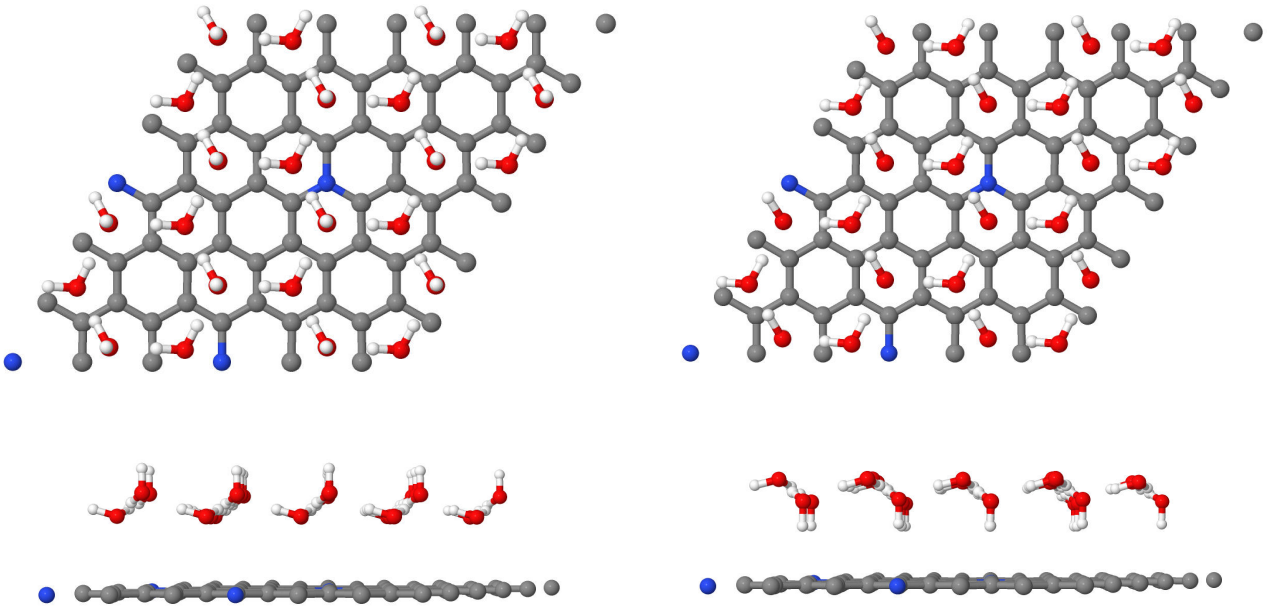

H-up H-down

Figure 13. "H-up" and "H-down" ice bilayer configurations on CN_x

Eighteen different rotational and translational configurations are possible for both the H-up and H-down structures, given that each oxygen atom is centered about one of the internal C-6 rings. Each of the possible conformations is considered in evaluating the stabilization effects by the formation of water clusters (E_{bind}) and the CN_x surface (E_{ads}). E_{bind} and E_{ads} are calculated by equations 4 and 5, respectively.

$$E_{bind} = E_{cluster} - 6E_{H2O} \quad (4)$$

$$E_{ads} = E_{surf+cluster} - (E_{surf} + E_{cluster}) \quad (5)$$

The parameters in these equations are the electronic energy calculations for an individual water molecule (E_{H2O}), a cluster of 6 water molecules ($E_{cluster}$), the bare surface (E_{surf}), and the surface-adsorbate complex ($E_{surf+cluster}$). Equations 4 and 5 are applied to the H-up and H-down water

bilayer configurations on CNx, as well as defect-free graphene, for comparison. The results of these calculations are included in Table 1. The CN_x-solvent adsorption energies are reported as the mean of the 18 samples (standard deviation is less than 0.0005 eV/molecule).

Table 1. H_2O adsorption and binding energies (eV/molecule H2O)

E_{bind}	$E_{ads,graphene - H up}$	$E_{ads, graphene - H down}$	$E_{ads, CNx - H up}$	$E_{ads, CNx - H down}$
-0.486	-0.066	-0.071	-0.073	-0.072

The results in Table 1 demonstrate the aforementioned hydrobicity of graphene, even with the inclusion of the nitrogen defect. This property of the surface may be deduced since the binding energy of the cluster is an order of magnitude larger than the adsorption energy of the cluster to the surface for each bilayer configuration. The adsorption energies for the cluster on CN_x are relatively consistent with the results for defect-free graphene. The findings from this work are qualitatively similar to work done elsewhere [32]. From these findings, it is concluded that the solvent structure is independent of the surface, and the maximum number of hydrogen bonds provides the greatest stabilization. Therefore, all 36 configurations of the solvent will be considered for the simulations with explicit solvent inclusion.

3.4 – Explicit Solvent Corrections

Each of the solvent bilayer configurations discussed previously are introduced into the unsolvated systems depicted in Figure 10. The system studied is the 3x3 unit cell in order to reduce computation time. It is hypothesized that the introduction of the solvent will reduce the solvent interactions from the periodic boundary, because of the newly formed adsorbate-water hydrogen bonding interactions following geometry optimization.

The free energy of each adsorbed intermediate is calculated to determine solvent dependence. However, since each of the 36 simulations begins in unique starting position, there exists a distribution of calculated energies. In Figure 14, histograms of these free energies (calculated relative to 4(H+ + e-) + O2 at 0 V-RHE) are included for each adsorbed intermediate. For each intermediate, there appears to be two distinct regions of concentration. In fact, these correspond to the simulations that start either in the H-up or H-down configuration.

Below the histograms in Figure 14 are results from an ANOVA analysis evaluating the significance of a discrete factor (starting configuration, H-up or H-down) on the free energy of each intermediate. For all three statistical tests, the null hypothesis is rejected, suggesting that the starting configuration is significant in determining the stability of the intermediate. The conclusion is therefore that the simulations that start with the solvent bilayer in the H-down configuration lead to the calculation of a more stable adsorbate. This may be attributed to the ease in forming new hydrogen bonds when there is already a hydrogen atom coordinated to the surface, and therefore the intermediate. Given these conditions the calculations are more likely to converge to an electronic energy that is closer to a PES global minimum than for the H-up simulations.

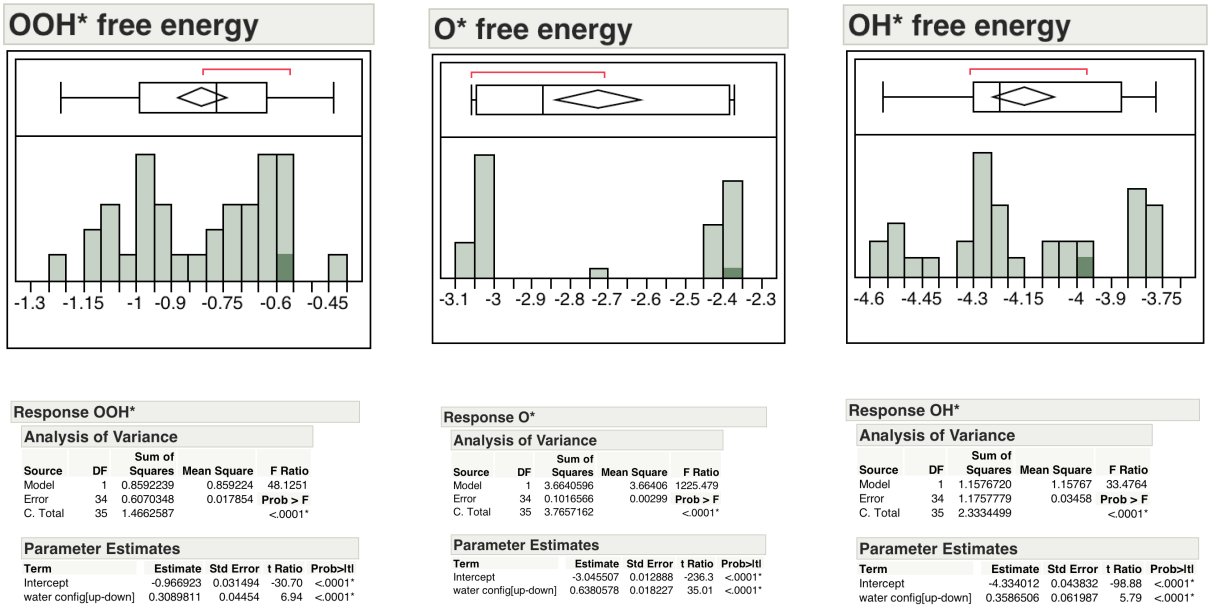

Figure 14. Discrete factor model relating initial water configuration to free energy

For each set of calculations, the most stable (lowest free energy relative to reactants) is used in generating the energy diagram to provide a prediction for the catalyst onset potential. The results are compiled, and corrected for potential-dependence in the free energy diagram in Figure 15. The results for the unsolvated calculations at 0 V-RHE are included in the figure as well to demonstrate the stabilization effects. These stabilization effects are listed in Table 2, alongside predictions from the literature [29-31] for comparison.

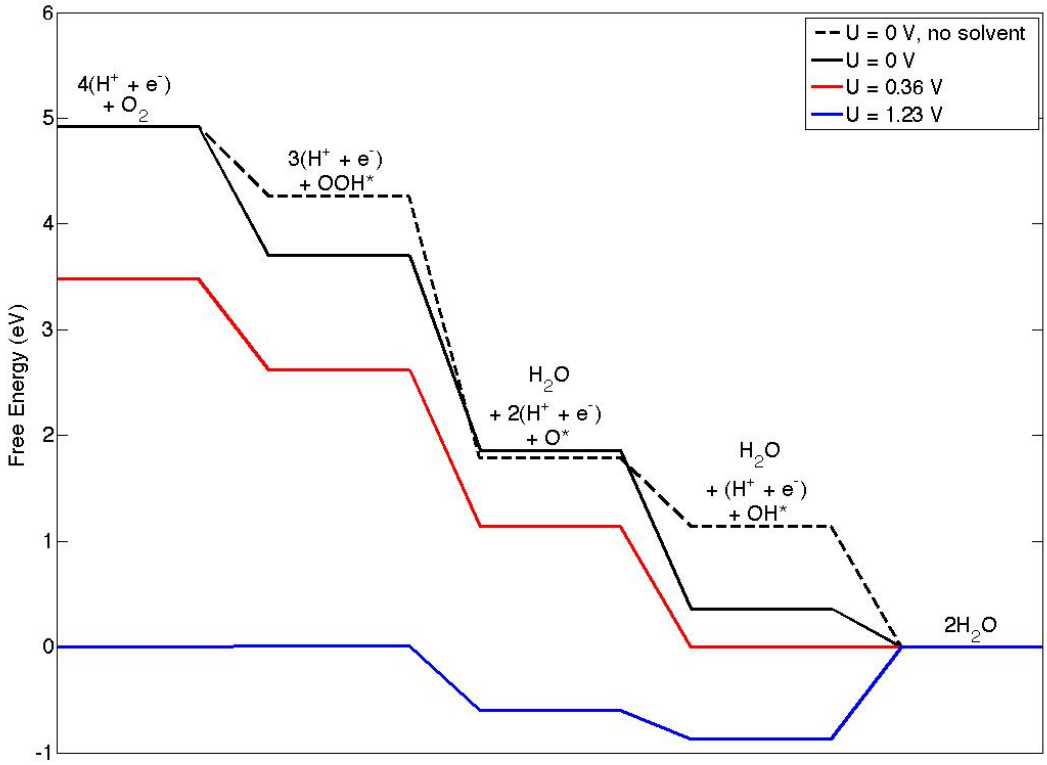

Figure 15. Free energy diagram including explicit solvent corrections

Table 2. Intermediate free energy stabilization from solvent effects (eV)		
Intermediate	Predicted[28,29,30]	Actual
OOH*	0.25	0.56
OH*	0.50	0.78

The results indicate that there is qualitative consistency between the predicted solvent stabilization effects and the results from the explicit inclusion of water. Although the stabilization effect is greater with the explicit inclusion of water, the trend of stabilization remains consistent: OH* is stabilized to a greater extent than OOH*, and the effect of solvent stabilization on the O* intermediate is negligible. The stabilization in these intermediates derives

from the formation of hydrogen bonding networks with the solvent bilayer. These hydrogen bonding networks can be seen for the adsorbed OOH* and OH* species in Figures 16 and 17, respectively.

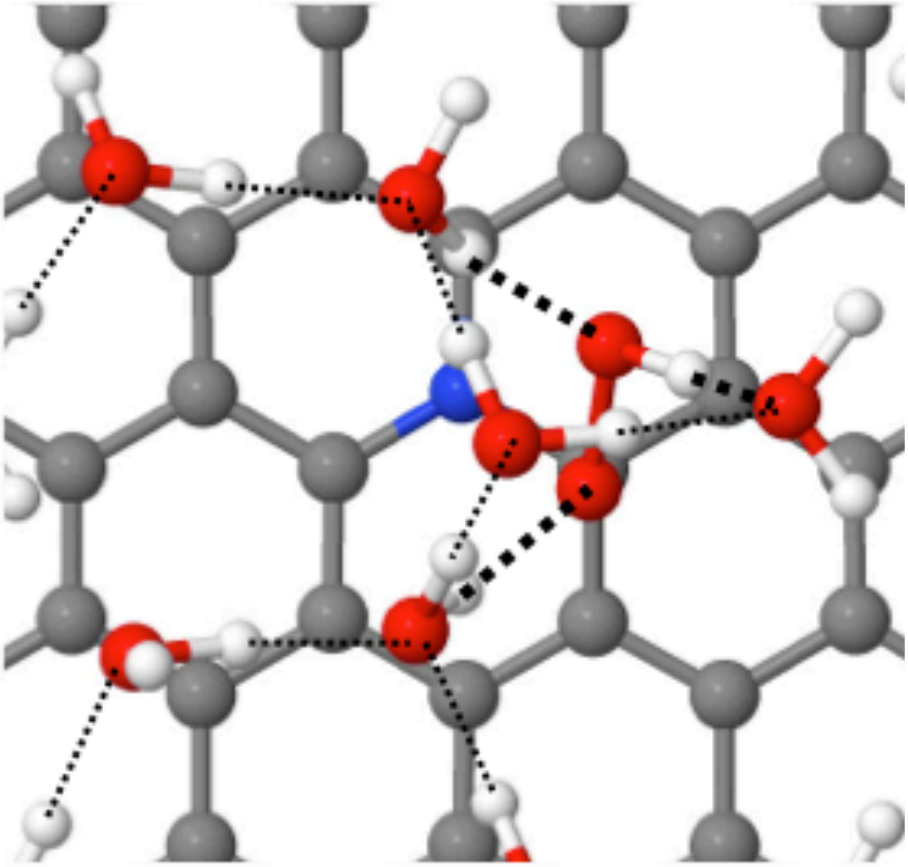

Figure 16. Hydrogen bonding network between solvent layer and adsorbed OOH*

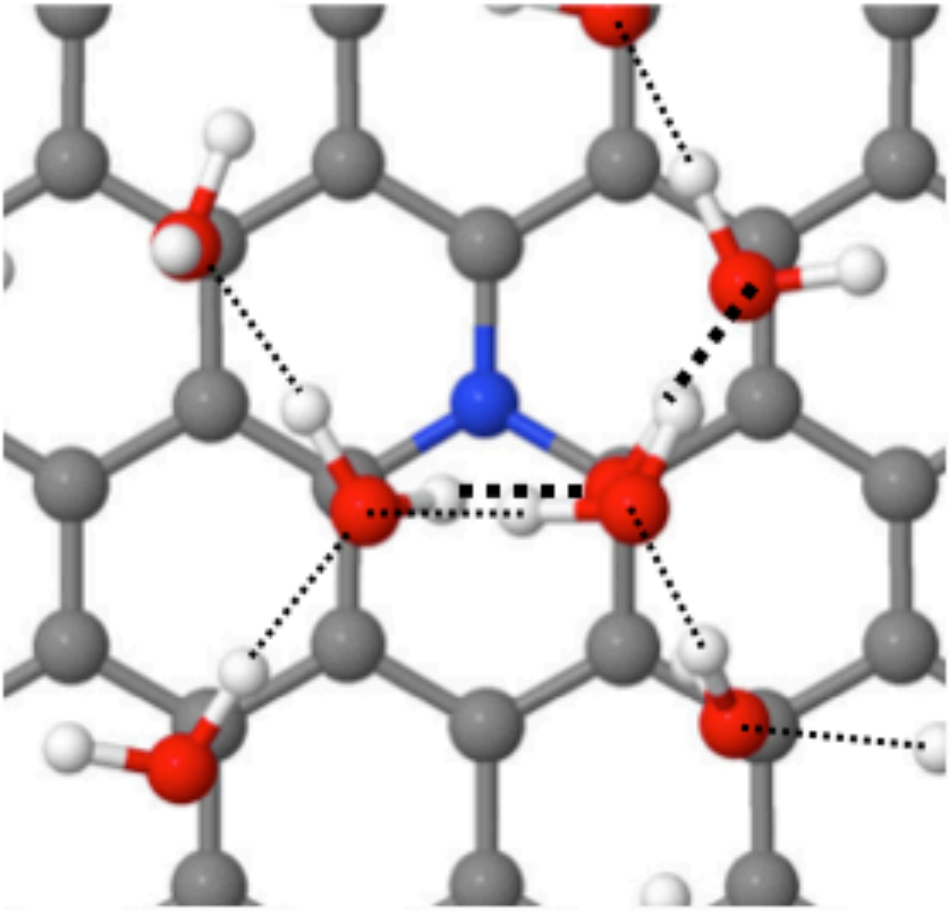

Figure 17. Hydrogen bonding network between solvent layer and adsorbed OH*

However, these stabilization effects do not succeed in lowering the predicted overpotential, as previously predicted [28]. As was the case with the implicit inclusion of stabilization effects, the overbound OH* specie leads to the final reduction step being the one which is rate-limiting. Since the stabilization effect is larger with the explicit inclusion of water molecules, the final reduction from OH* to H_2O occurs at a lower onset potential, leading to a higher predicted overpotential for the catalyst.

4. Discussion

4.1 – Summary of Results

The ORR was studied on CNx materials with the explicit inclusion of water molecules in order to understand the effect of solvent on the stability of reaction intermediates and the predicted catalyst activity. Through a study of the structure of water at the surface interface, the hydrophobicity of graphene found in previous experimental and theoretical work is demonstrated through DFT simulations. The surface properties with respect to water molecule remain consistent when the nitrogen defect is included into graphene, as well.

The solvent structure facilitated a systematic study of its role on the stabilization of the intermediates observed in the reaction scheme. The initial configuration of the solvent bilayer was shown to be statistically significant, as the H-down configuration is able to readily form new hydrogen bonds and relaxes to an optimized geometries that is more true to the global PES minimum electronic energy than in the H-up configuration. The results from this study allowed for comparison to the hypothesized stabilization effects and generated the data necessary to predict the activity of the catalyst.

The predicted overpotential and rate-limiting steps for each system in this study are included in Table 3, along with results from previous computational ORR work on CN^x and Pt(111).

Table 3. Predicted catalyst ORR overpotential and rate-limiting step.		
Model	Overpotential ($\eta = U_0 - U$)	rate-limiting step
CN_x - 6x6 cell, no solvent	0.58	OOH* formation / O* reduction to OH* (tie)
CN_x - 6x6 cell, constant solvent correction	0.59	OH* reduction to H_2O
CN_x - 3x3, explicit solvent inclusion	0.87	OH* reduction to H_2O
CN_x - Studt [28]	0.72	O* reduction to OH*
Pt(111) [29]	0.45	O* reduction to OH* / OH* reduction to H_2O (tie)

The 6x6 cells without solvent inclusion and with implicit solvent corrections show good agreement with the predicted overpotential from the Studt work on a similar system [28]. However, with explicit solvent inclusion the predicted overpotential is quite high. However, this result is expected to a certain extent since experiment suggests that the graphitic nitrogen dopant patterns investigated in this work do not contribute to significant catalytic properties for the ORR. The active site for these CNx materials is likely derivative of nitrogen doping near the edges of the graphene sheet [16,46].

4.2 - Implications

Although the results of this work do not allow for direct support of experimental activity testing, the insight provided by the study of solvation effects in the theoretical model is important for future computational work on these materials. The results suggest that although, the trend of solvent stabilization effects remains consistent with previous work on metal catalysts, quantifying these stabilization effects may only be achievable through the explicit inclusion of water in the model. The methodologies used in this work will be useful for the development of useful theoretical models that are able support experimental observations for the ORR on CN_x materials.

5. Future Directions

5.1 – Edge Defects

Experimental work indicates that the edge sites of CNx materials are likely candidates for the catalytically active site [15,16]. However, it is unclear what type of nitrogen doping pattern near the edge is associated with the most active site for the ORR. Several possible doping patterns are illustrated in Figure 18. The nitrogen doping patterns included in the figure are quaternary graphitic (N0), pyridinic (Py), hydrogen-terminated pyridinic (Py-H), and oxygen-terminated pyridinic (Py-O). Additonal doping patterns are possible, such as graphitic substitutions farther away from the graphene sheet edges. However, these are not likely candidates for the active site [45].

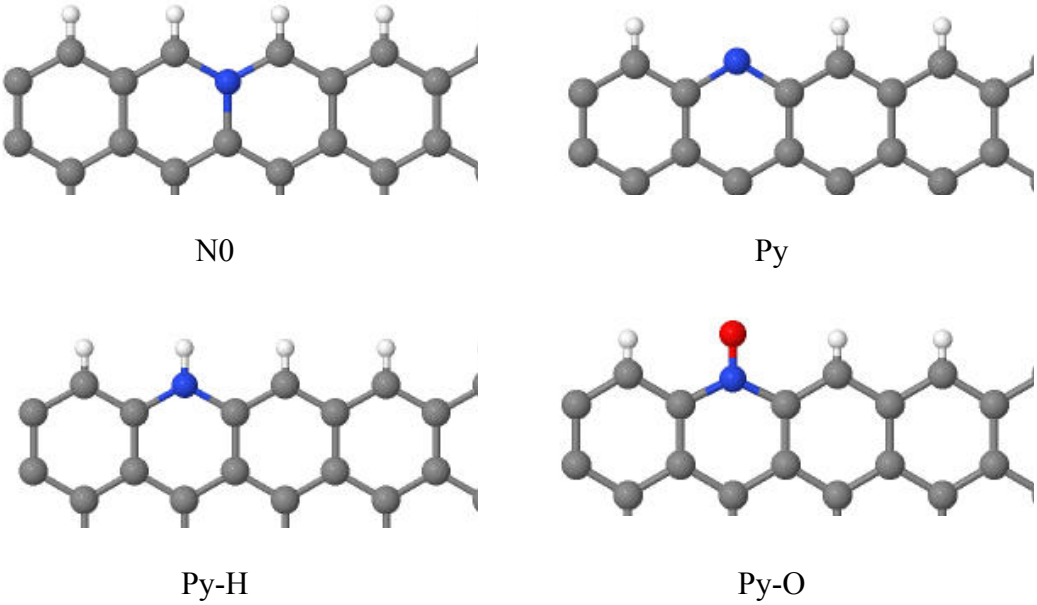

Figure 18. Possible N-doping patterns at graphene edges.

Preliminary calculations are performed for each ORR intermediate species at the most stable adsorption site for the four doping patterns considered in Figure 18. These simulations are carried out in the absence of solvent, through the methodology discussed in Section 3.1. Free energies of the OOH* and OH* intermediates are corrected implicitly, by factors of 0.25 eV and 0.50 eV, respectively. The predicted overpotentials for each of these systems are included in Table 4, with and without solvent corrections. The quaternary-N edge-doping pattern is predicted to be most active for the ORR, given the results. The free energy diagram in Figure 19 describes the reaction pathway on CN_x with this edge defect.

Table 4. Predicted overpotential (V) for various graphene edge defects		
	No solvent	Implicit correction [28-30]
N0	0.67	0.88
Py	0.62	1.12
Py-H	1.62	1.37
Py-O	0.41	0.91

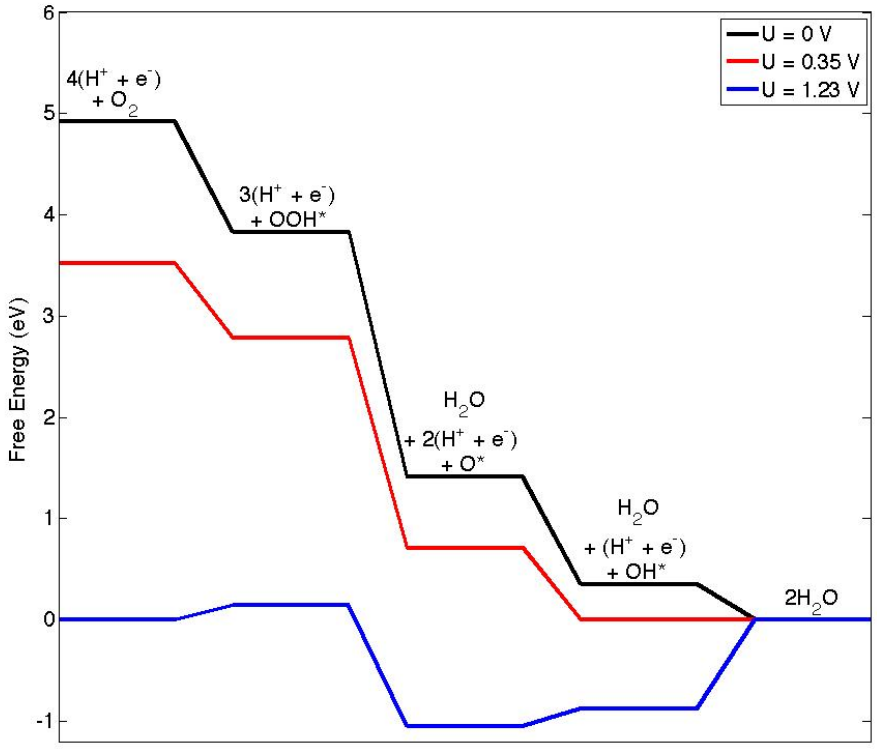

Figure 19. Free energy diagram for N0 edge defect with constant solvent correction

This result appears to contradict the initial experimental work from Ozkan and co-workers. This study suggested that the greatest activity is observed in CNx materials as a result of pyridinc-N doping. It is mentioned that though characterization suggests pyridinic edge structures, the results may just be an indication of edge plane exposure [16].

Results from previous computational work observe low adsorption barriers and a favorable reaction pathway on graphene structures with quaternary-N defects. The initial evaluations of the activity of these structures towards the ORR agree with these findings. Additionally, the proposed mechanistic ring opening at the O* state of the reaction pathway is observed in this work [45]. A graphic of this ring-opened structure on the quaternary-N CN_x surface is pictured in Figure 20. The ring opening exposes a pyridinic species, which may provide support for the identification of pyridinic structure during characterization [16].

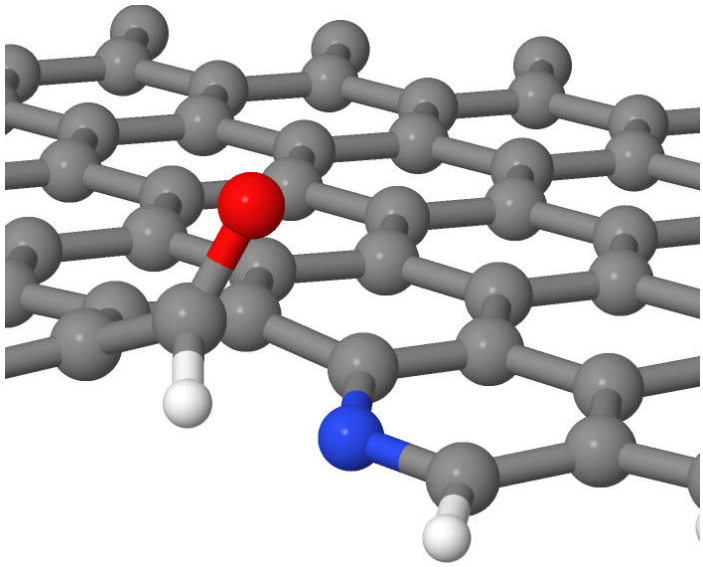

Figure 20. Ring-opening mechanism, exposing a pyridinic edge

The initial calculations on the CN_x edge sites are able to support previous experimental and computational research. However, the extension of the explicit solvent inclusion model to these systems is necessary to understand how this may impact the predicted catalytic activity. An understanding of the ORR mechanism near CN_x edge sites may provide insight for observable properties from experiment, and may facilitate the design of efficient CN_x-based materials from the molecular level.

5.2 – Integrating metals into CN_x Materials

Much debate regarding the source of ORR activity of CN_x materials centers on the presence of metals in the structure. These residual components may be left over due to insufficient acid wash. The integration of cobalt and nickel into CN_x has been studied through DFT simulations for these reasons [18,19]. A Co-N_4 graphene defect is pictured in Figure 21. The integration of metals into these materials shows much promise for robust catalytic materials. Recent work on the ORR activity on an Fe-C-N catalysts demonstrates excellent stability, selectivity and activity. The properties of these materials are reported to be comparable, if not superior to, the commercial Pt/C ORR catalyst [46]. The atomistic study of CN_x materials with the integration of various transition metals may provide insight to experimentalists as to which transition metals may present promising catalytic materials.

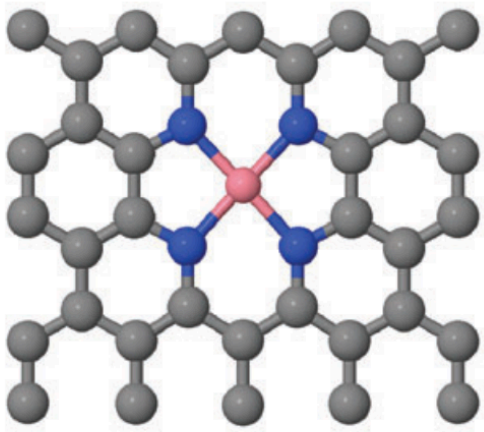

Figure 21. Graphitic Co-N_4 defect [18]

5.3 – Alternate Heteroatoms

The doping of graphene with alternate heteroatoms has been achieved through experimental synthesis, with some materials showing activity for oxygen reduction. The source of CN_x activity is the more electronegative nitrogen atom pulling electron density from carbon atoms, which makes the adsorption energy of each intermediate favorable. Through volcano plots, many studies identify that the ORR activity of a catalyst is often found to be a strong function of the O* adsorption energy [29,47]. Thus, choosing heteroatoms that are able to tune these adsorption energies accordingly may provide a pathway to identifying a strong ORR catalyst candidate. Several alternate heteroatoms have shown to have ORR activity through experimental observation, including sulfur [48], phosphourus [49], and boron [50]. The analysis of these heteroatoms among others may provide predictive capabilities of oxygen reduction activity as a function of the non-metal heteroatom dopant properties.

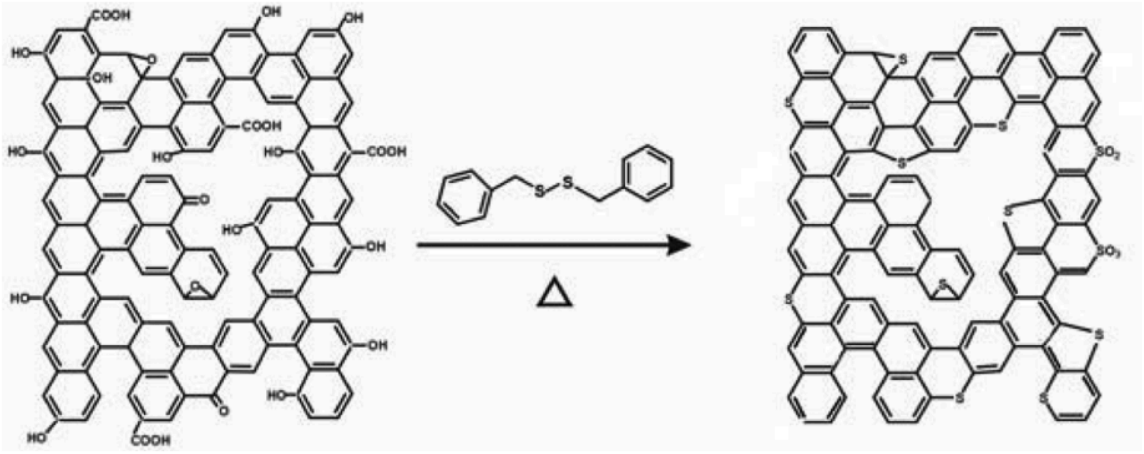

Figure 22. Sulfur-doped graphene synthesis [48]

6. Conclusions

The explicit inclusion of water molecules are integrated into DFT simulations of the ORR on a CN_x surface. The results demonstrate the stabilization effects of the solvent bilayer on the OOH* and OH* intermediates in the reaction scheme. Though these effects follow similar trends for the implicit models developed previously, the magnitude of these corrections is greater by about 0.50 eV for each intermediate. The predicted catalyst overpotential is increased with these solvent corrections due to increased stabilization effects added to the overbound OH* intermediate. The methodologies for the explicit inclusion of solvent in modeling electrochemical reactions may be applied to similar systems. The extension of these methods to various nitrogen doping patterns may be able to confirm experimental results and would be indicative of a robust model. Further development of these techniques will be important to better understand the ORR mechanism on these materials, and to motivate molecular level design and analysis of efficient catalytic materials.

References

1. Hubbert, M. K., Nuclear Energy and the Fossil Fuels. American Petroleum Institute Spring Meeting: San Antonio, 1956.
2. Olah, G. A., Prakash, G. K. S., Goeppert, A., Anthropogenic Chemical Carbon Cycle for a Sustainable Future. *J. Am. Chem. Soc.* **2011**, 133(33): 12881-12898.
3. Environmental Protection Agency. Overview of Greenhouse Gases. http://www.epa.gov/climatechange/ghgemissions/gases/co2.htm
4. Scripps Institution of Oceanography. The Keeling Curve. http://www.thekeelingcurve.uscd.edu (accessed Mar 24, 2014).
5. Nie, X., Esopi, M. R., Janik, M. J., Asthagiri, A. R., Selectivity of CO2 Reduction on Copper Electrodes: The Role of the Kinetics of Elementary Steps. *Angew. Chem. Int. Ed.* **2013**, 52(9): 2459-2462.
6. Steele, B. C. H., Heinzel, A. Materials for fuel-cell technologies. *Nature* **2001**, 414: 345- 352.
7. Cleghorn, S. J. C., Ren, X., Springer, T. E., Wilson, M. S., Zawodowski, C., Zawadowski, T. A., Gottesfield, S. PEM fuel cells for transportation and stationary power generation applications. *Int. J. Hydrogen Energy* **1997**, 22 (12): 1137-1144.
8. Environmental Protection Agency. Fuel Cells & Vehicles: Basic Information. http://www.epa.gov/otaq/fuelcell/basicinfo.htm (accessed Mar 24, 2014).
9. Rossmeisl, J., Qu, Z.-W., Zhu, H., Kroes, G.-J., Nørskov, J. K., Electrolysis of water on oxide surfaces. *J. Electroanal. Chem.* **2007**, 607 (1-2): 83-89.
10. Janik, M. J., Taylor, C. D., Neurock, N. First-principles analysis of the initial electroreduction steps of oxygen over Pt(111). *J. Electrochem. Soc.* **2009**, 156: B126-B135.
11. Klee, R. J., Graedel, T. E., Elemental Cycles: A Status Report on Human or Natural Dominance. *Annu. Rev. Environ. Resour.* **2004**, 29: 69-107.
12. Rabis, A., Rodriguez, P., Schmidt, T. J., Electrocatalysts for Polymer Electrolyte Fuel Cells: Recent Achievements and Future Challenges. *ACS Catal*. **2012**, 2: 864-890.
13. Greeley, J., Stephens, I. E. L., Bondarenko, A. S., Johansson, T. P., Hansen, H. A., Jaramillo, T. F., Rossmeisl, J., Chorkendorff, I., Nørskov, J. K. Alloys of platinum and early transition metals as oxygen reduction electrocatalysts. *Nature Chem.* **2009**, 1: 552-556.
14. Qu, L., Liu, Y., Baek, J-B., Dai, L. Nitrogen-Doped Graphene as Efficient Metal-Free Electrocatalyst for Oxygen Reduction in Fuel Cells. *ACS Nano* **2010**, 4 (3): 1321-1326.
15. Geng, D., Chen, Y., Chen, Y., Li, Y., Sun, X., Ye, S., Knights, S. High oxygen-reduction activity and durability of nitrogen-doped graphene. *Energy Environ. Sci.* **2011**, *4*: 760-764.
16. Matter, P. H., Zhang, L., Ozkan, U. S. The role of nanostructure in nitrogen-containing carbon catalysts for the oxygen reduction reaction. *J. Catal.* **2006**, 239: 83-96.
17. Bao, X., Nie, X., von Deak, D., Biddinger, E. J., Luo, W., Asthagiri, A., Ozkan, U. S., Hadad, C. M., A first-principles study of the role of quaternary-N doping on the oxygen reduction activity and selectivity of graphene edge sites. *Top. Catal.* **2013**, 1-11.

18. Kattel, S., Atanassov, P., Kiefer, B. Catalytic activity of Co-N_x/C electrocatalysts for oxygen reduction reaction: a density functional theory study. *Phys. Chem. Chem. Phys.* **2013**, 15: 148-153.
19. Kattel, S., Atanassov, P., Kiefer, B. Density Functional Theory Study of Ni-N_x/C Electrocatalyst for Oxygen Reduction in Alkaline and Acidic Media. *J. Phys. Chem. C.* **2012**, 116 (33): 17378-17383.
20. Matter, P. H., Wang, E., Arias, M., Biddinger, E. J., Ozkan, U. S. Oxygen reduction reaction catalysts prepared from acetonitrile pyrolysis over alumina-supported metal particles. *J. Phys. Chem. B.* **2006**, 110: 18374-18384.
21. Matter, P. H., Wang, E., Ozkan, U. S. Preparation of nanostructured nitrogen-containing carbon catalysts for the oxygen reduction reaction from SiO_2 and MgO-supported metal particles. *J. Catal.* **2006**, 243: 395-403.
22. Matter, P. H., Ozkan, U. S. Non-metal catalysts for dioxygen reduction in an acidic electrolyte. *Catal. Lett.* **2006**, 109: 115-123.
23. Matter, P. H., Wang, E., Millet, J-M. M., Ozkan, U. S. Characterization of the iron phase in CN_x-based oxygen reduction reaction catalysts. *J. Phys. Chem. C.* **2007**, 111: 1444-1450.
24. Matter, P. H., Wang, E., Arias, M., Biddinger, E. J., Ozkan, U. S. Oxygen reduction reaction activity and surface properties of nano-structured nitrogen-containing carbon. *J. Mol. Catal. A. Chem.* **2007**, 264: 73-81.
25. Biddinger, E., von Deak, D., Ozkan, U. S. Nitrogen containing carbon nanostructures as oxygen-reduction catalysts. *Top. Catal.* **2009**, 52: 1566-1574.
26. Gong, K., Du, F., Xia, Z., Durstock, M., Dai, L., Nitrogen-Doped Carbon Nanotube Arrays with High Electrocatalytic Activity for Oxygen Reduction. *Science* **2009**, 323(5915): 760-764.
27. Zheng, Y., Jiao, Y., Chen, J., Liu, J., Liang, J., Du, A., Zhang, W., Zhu, Z., Smith, S. C., Jaroniec, M., Lu, G. Q., Qiao, S. Z., Nanoporous Graphitic-C3N4@Carbon Metal-Free Electrocatalysts for Highly Efficient Oxygen Reduction. *J. Am. Chem. Soc.* **2011**, 133(50): 20116-20119.
28. Studt, F., Oxygen reduction reaction on nitrogen-doped graphene. *Catal. Lett.* **2013**, 143: 58-60.
29. Nørkov, J. K., Rossmeisl, J., Logadottir, A., Lindqvist, L., Kitchin, J. R., Bilgaard, T., Jónsson, H., Origin of the Overpotential for Oxygen Reduction at a Fuel-Cell Cathode. *J. Phys. Chem. B.* **2004**, 108: 17886-17892.
30. Tripković, V., Skúlason, E., Siahrostami, S., Nørkov, J. K., Rossmeisl, J., The oxygen reduction reaction mechanism on Pt(111) from density functional theory calculations. *Electrochim. Acta.* **2010**, 55(27): 7975-7981.
31. Karlberg, G. S., Wahnström, G., Density-Functional Based Modeling of the Intermediate in the Water Production Reaction on Pt(111). *Phys. Rev. Lett.* **2004**, 92(13): 136103.
32. Kresse, G., Hafner, J., *Ab initio* molecular dynamics for liquid metals. *Phys. Rev. B.* **1993**, 47(1): 558-561.
33. Kresse, G., Hafner, J., *Ab initio* molecular-dynamics simulation of the liquid-metal-amorphous-semiconductor transition in germanium. *Phys. Rev. B.* **1994**, 49(20): 14251.

34. Kresse, G., Furthmüller, J., Efficient iterative schemes for *ab initio* total-energy calculations using a plane-wave basis set. *Phys. Rev. B.* **1996**, 54: 11169-11186.
35. Kresse, G., Furthmüller, J., Efficiency of *ab-initio* total-energy calculations for metals and semiconductors using a plane-wave basis set. *Comput. Mater. Sci.* **1996**, 6(1): 15-50.
36. Kresse, G., Joubert, D., From ultrasoft psuedopotentials to the projector augmented-wave method. *Phys. Rev. B.* **1999**, 59: 1758-1775.
37. Blöchl, P. E., Projector augmented-wave method. *Phys. Rev. B.* **1994**, 50: 17953-17979.
38. Perdew, J. P., Burke, K., Ernzerhof, M., Generalized Gradient Approximation Made Simple. *Phys. Rev. Lett.* **1996**, 77: 3865-3868.
39. Leenaerts, O., Partoens, B., Peeters, F. M., Adsorption of H2O, NH3, CO, NO2, and NO on graphene: A first-principles study. *Phys. Rev. B.* **2008**, 77: 125416.
40. Leenaerts, O., Partoens, B., Peeters, F. M., Water on graphene: Hydrophobicity and dipole moment using density functional theory. *Phys. Rev. B.* **2009**, 79(23): 235440.
41. Voloshina, E., Usvyat, D., Schütz, M., Dedkov, Y., Paulus, B., On the physisorption of water on graphene: A CCSD(T) study. *Phys. Chem. Chem. Phys.* **2011**, 13: 12041-12047.
42. Grimme, S., Antony, J., Ehrlich, S., Krieg, H., A consistent and accurate *ab initio* parameterization of density functional dispersion correction (DFT-D) for the 94 elements H-Pu. *J. Chem. Phys.* **2010**, 132: 154104.
43. González, B. S., Hernández-Rojas, J., Bretón, J., Gomez Llorente, J. M., Global Potential Energy Minima of (H2O)n Clusters on Graphite. *J. Phys. Chem. C.* **2007**, 111: 14862-14869.
44. Schedin, F., Geim, A. K., Morozov, S. V., Hill, E. W., Blake, P., Katsnelson, M. I., Novoselov, K. S., Detection of individual gas molecules adsorbed on graphene. *Nat. Mater.* **2007**, 6: 652-655.
45. Kim, H., Lee, K., Woo, S. I., Jung, Y., On the mechanism of enhanced oxygen reduction reaction in nitrogen-doped graphene nanoribbons. *Phys. Chem. Chem. Phys.* **2011**, 13(39): 17505-17510.
46. He, C., Zhang, J. J., Shen, P. K., Nitrogen-self-doped graphene non-precious metal catalyst with superior performance to Pt/C catalyst toward oxygen reduction reaction. *J. Mater. Chem. A* **2014**, 2: 3231-3236.
47. Stamenkovic, V., Mun, B. S., Mayrhofer, K. J. J., Ross, P. N., Markovic, N. M., Rossmeisl, J., Greeley, J., Nørkov, J. K., Changing the Activity of Electrocatlysts for Oxygen Reduction by Tuning the Surface Electronic Structure. *Angew. Chem.* **2006**, 118(18): 2963-2967.
48. Yang, Z., Yao, Z., Li, G., Fang, G., Nie, H., Liu, Z., Zhou, X., Chen, X., Huang, S., Sulfur-Doped Graphene as an Efficient Metal-free Cathode Catalyst for Oxygen Reduction. *ACS Nano* **2012**, 6(1): 205-211.
49. Liu, Z-W., Peng, F., Wang, H-J., Yu, H., Zheng, W-X., Yang, J., Phosphourus-Doped Graphite Layers with High Electrocatalytic Activity for the O_2 Reduction in Alkaline Medium. *Angew. Chem.* **2011**, 123(14): 3315-3319.
50. Sheng, Z-H., Gao, H-L., Bao, W-J., Wang, F-B., Xia, X-H., Synthesis of boron doped graphene for oxygen reduction in fuel cells. *J. Mater. Chem.* **2012**, 22: 390-395.